



HAL
open science

Denudation outpaced by crustal thickening in the eastern Tianshan

Julien Charreau, Dimitri Saint-Carlier, Stephane Dominguez, Jérôme Lavé, P. Blard, Jean-Philippe Avouac, Marc Jolivet, Yan Chen, Shengli Wang, David. Nathan Brown, et al.

► To cite this version:

Julien Charreau, Dimitri Saint-Carlier, Stephane Dominguez, Jérôme Lavé, P. Blard, et al.. Denudation outpaced by crustal thickening in the eastern Tianshan. *Earth and Planetary Science Letters*, 2017, 479, pp.179-191. 10.1016/j.epsl.2017.09.025 . insu-01610154

HAL Id: insu-01610154

<https://insu.hal.science/insu-01610154v1>

Submitted on 28 Nov 2019

HAL is a multi-disciplinary open access archive for the deposit and dissemination of scientific research documents, whether they are published or not. The documents may come from teaching and research institutions in France or abroad, or from public or private research centers.

L'archive ouverte pluridisciplinaire **HAL**, est destinée au dépôt et à la diffusion de documents scientifiques de niveau recherche, publiés ou non, émanant des établissements d'enseignement et de recherche français ou étrangers, des laboratoires publics ou privés.

1 The Tianshan range, an example of an immature orogenic
2 wedge? Evidence from active deformation and denudation
3 rates within the intermontane basins

4 Julien Charreau¹, Dimitri Saint-Carlier¹, Stéphane Dominguez², Jérôme Lavé¹, Pierre-Henri
5 Blard¹, Jean-Philippe Avouac³, Marc Jolivet⁴, Yan Chen⁵, ShengLi Wang⁶, Nathan David
6 Brown⁷, Luca Claude Malatesta³, Edward Rhodes⁷, and ASTER Team^{8*}

7 ¹ Université de Lorraine, CRPG, UMR 7358 CNRS-UL, 15 rue Notre Dame des Pauvres, 54501
8 Vandœuvre lès Nancy, France

9 ² Université de Montpellier, Géosciences Montpellier, UMR 5243, Place E. Bataillon, 34095
10 Montpellier Cedex 5, France

11 ³ California Institute of Technology, Division of Geology and Planetary Sciences, 1200 E California
12 Blvd, Pasadena CA 91125, United States

13 ⁴ Université de Rennes, Géosciences Rennes, UMR 6118, Campus de Beaulieu 35042 Rennes, France

14 ⁵ Université d'Orléans, Institut des Sciences de la Terre d'Orléans, UMR 7327, Campus Géosciences,
15 45071 Orléans, France

16 ⁶ Nanjing University, Department of Earth and Sciences, Nanjing, China

17 ⁷ University of California, Department of Earth, Planetary and Space Sciences, Los Angeles,
18 California 90095-1567, United States

19 ⁸ Université Aix-Marseille, CNRS-IRD-Collège de France, UM 34 CEREGE, Technopôle de
20 l'Environnement Arbois-Méditerranée, 13545 Aix-en-Provence, France

21 * M. Arnold, G. Aumaître, D.L. Bourlès, K. Keddadouche

22

23 Keywords: Tianshan; ¹⁰Be exposure dating; shortening rates; Intermontane basin; Bayanbulak basin;
24 relief dynamics; mountain building; active tectonics

25

26 **ABSTRACT**

27 The modern Tianshan mountain range resulted from the reactivation of a Paleozoic
28 orogenic belt in response to the India/Asia collision and today the range exhibits high
29 topography, tectonically active forelands, and intermontane basins. The distribution of crustal
30 shortening across the range is likely controlled by inherited Paleozoic structures.. Based on
31 quantitative morphotectonic observations and age constraints derived from cosmogenic ¹⁰Be
32 dating, single-grain post-infrared infrared stimulated luminescence (p-IR IRSL) dating and
33 modeling of fault scarp degradation, we have quantified the deformation in the Nalati and

34 Bayanbulak intermontane basins in the central Eastern Tianshan. Our results indicate that at
35 least 1.4mm/yr of horizontal crustal shortening is accommodated within these two basins.
36 This shortening represents a significant portion (>15 %) of the 8.5 ± 0.5 mm/yr total shortening
37 rate across the entire range at this longitude. Accordingly, the Eastern Central Tianshan is
38 thickening at a mean rate of ~ 1.4 mm/yr, a rate that is significantly higher than the average
39 denudation rate of 0.14 mm/yr derived from our cosmogenic analysis. This discrepancy
40 suggests that the Tianshan range has not yet reached a steady topography and remains in a
41 transient state of topographic growth, most likely due to the arid climate, which limits the
42 denudation rates.

43

44 1. INTRODUCTION

45 Intracontinental orogenic belts typically form single or double vergent prisms that
46 grow from a combination of frontal accretion and underplating (e.g. Willett et al., 2001). In
47 the presence of denudation, a topographic steady-state can be reached in which denudation
48 balances crustal thickening (J. Avouac and Burov, 1996; Dahlen and Suppe, 1988; Willett et
49 al., 2001). This could result from either crustal shortening of the internal part of the range or
50 underplating due to an accumulation of material which is then thrust under the wedge. The
51 resulting balanced topography generally has a simple asymmetric triangular shape, with
52 steeper slopes on the windward side of the range (Willett et al., 2001).

53 Here, we investigate the Eastern Tianshan in central Asia (Fig. 1), whose topography
54 differs from these classical profiles (Fig. A) even though it is one of the largest and most
55 active intracontinental orogenic belts in the world. The range is composed of a series of
56 elevated ranges (> 4000 m) separated by very large E–W striking intermontane basins such as
57 the Yili, Bayanbulak, Nalati, Turpan and Yanqi basins (Fig. 1). How this particular
58 topography is growing, and especially whether or not it has reached a steady state, are
59 questions that remain unresolved.

60 Present-day shortening rates, derived from GPS measurements across the entire range,
61 reach 20 mm/yr in the western Tianshan and decrease progressively eastward, to a value of
62 8.5 ± 0.5 mm/yr at the longitude of this study and to even lower rates further east (e.g. Reigber
63 et al., 2001; Yang et al., 2008). Because of the presence of inherited Paleozoic structures, this
64 shortening is not focused on the boundaries but is instead distributed across the entire range,
65 and significant evidence for active deformation is observed within the central part of the range
66 (Jolivet et al., 2010; Poupinet et al., 2002; Thompson et al., 2002; Wu et al., 2014). In the
67 eastern part of the range, the amount and rate of internal deformation remains poorly
68 constrained (Jolivet et al., 2010; Wu et al., 2014). Recent denudation rates on both sides of the
69 range are relatively low (0.2–0.4 mm/yr) (Guerit et al., 2016; Jolivet et al., 2010; Puchol et al.,
70 2016). Over the long term, because Cenozoic denudation is very limited, even low
71 temperature thermochronometers are of limited use in documenting the recent exhumation
72 history of the range, except for within the most active zones (Dumitru et al., 2001; Jolivet et
73 al., 2010). To better understand how the Tianshan is growing and to determine whether this
74 range has reached steady-state topography, more quantitative constraints on the distribution of
75 deformation across the range and its evolution through time, as well as estimates of the
76 associated denudation, are required, especially in the inner regions.

77 This study focuses on the Central Eastern Tianshan and investigates recent tectonics in
78 the Bayanbulak and surrounding Nalati and Yili intermontane basins (Fig. 1). Evidence
79 for active tectonics in this region has been reported but is poorly quantified. Here, we use
80 different techniques to quantify deformation and denudation rates. We demonstrate that
81 crustal thickening outpaces denudation and conclude that, despite its long geological history
82 and high topography, the Tianshan range is still in an early stage of topographic growth due to
83 the extremely low erosion rates in the region.

84

85 **2. GEOLOGICAL SETTING AND EVIDENCE FOR ACTIVE DEFORMATION IN THE**
86 **INTERMONTANE BASINS**

87 After a long Paleozoic geological history, the numerous intermontane basins were
88 created by a post-orogenic phase of transtensive deformation during the Permian to Late
89 Triassic (Charvet et al., 2007; Jolivet et al., 2010). These basins are still partially preserved,
90 though the range was strongly rejuvenated and shortened in the Late Cenozoic in response to
91 the India/Asia collision (e.g. Tapponnier and Molnar, 1979), which continues today.

92 The Bayanbulak, Nalati and Yili basins are large intermontane troughs, situated ~1500
93 to ~2400 m.a.s.l. (Fig. 1B) and surrounded by high elevation ranges with peaks at > 4000 m
94 composed mainly of Paleozoic meta-sedimentary and igneous basement (Fig. 1C).

95 The Bayanbulak basin is located between the South Tianshan range to the south and the
96 Narat range to the north. The northern edge of the basin exhibits clear evidence for recent
97 deformation along several northward-dipping E–W trending parallel stepped faults and
98 associated ~10 km long topographic scarps (Figs. 1C, 2, 3 and 4). These faults deform
99 numerous alluvial fan surfaces that were abandoned by southward flowing rivers that drain
100 the Narat range (Figs. 2 and 3).

101 Located to the north, the Nalati basin is a relatively small basin trapped within the
102 northern piedmont of the Narat Range and bound to the north by the >2000 m high Nalati
103 range. At least two parallel reverse faults, trending roughly E–W and dipping to the south, can
104 also be mapped within this basin (Fig. 5). The first lies at the base of the main reliefs of the
105 Narat Range and affects Quaternary glacial deposits. The second of these faults clearly offsets
106 the most recent alluvial sediments of the Nalati Basin (Fig. 5).

107 The Yili basin lies at a lower elevation north of the Nalati range and is limited to the
108 north by the Borohoro range. The basin is relatively narrow in the east but rapidly widens
109 toward the west in Kazakhstan. High E–W striking topographic steps can be observed along
110 its southern border (Fig. 5D). The nearby E–W flowing Yili river located at the center of the

111 basin might also have left E–W striking terrace risers, and thus the tectonic origin of the
112 topographic steps might be questioned. However, the presence of reverse and convex slopes is
113 suggestive of a tectonic origin.

114

115 **3. SHORTENING ESTIMATES**

116 3.1 Method

117 To quantify the amount of shortening across these active thrust faults, we determined
118 the vertical throw by measuring the vertical offset of the morphological markers. A Trimble
119 DGPS topographic device was used to acquire high resolution topographic measurements of
120 the markers. The elevation was then corrected from the regional slope estimated at each study
121 site, and the offset was measured directly on the corrected profiles. We considered a
122 conservative uncertainty of 15 % on the total vertical throw to account for morphological
123 roughness and horizontal advection of the regional slopes. The vertical throw was then
124 converted into a horizontal component of slip using the fault dip angle. Because of poor
125 outcrop conditions and the lack of subsurface geophysical data, we also assumed a fault dip
126 angle of $35\pm 10^\circ$ based on outcropping faults measured in the east of the Bayanbulak basin by
127 Jolivet et al. (2010) and Wu et al. (2014). We assume that all of the faults studied are pure
128 thrust faults as they strike approximately perpendicular to the azimuth of geodetic shortening
129 across the range (Fig. 1) and because the strike-slip component appears to be mostly second
130 order, at least in the basins studied (Wu et al., 2014).

131

132 3.2 Study sites and results

133 In the Bayanbulak basin, five sites were analyzed, numbered 1 to 5 from south to
134 north. Site BBK1 is located roughly ~20 km south of Bayanbulak city, where the Kaidu River
135 entrenches a large E–W trending anticline, abandoning two levels of fluvial terraces (Fig. 2).

136 The anticline is bordered to the south by a north-verging thrust (F1) that has deformed the
137 abandoned terraces. To the northwest, site BBK2 lies at the base of the Narat Range, where a
138 second E–W trending fault (F2) offsets a large alluvial fan that was later overlain by a
139 younger fan at the base of the fault (Fig. 2). Two sites (BBK3 and BBK4) located roughly 25
140 km east of BBK2 were also studied at the base of the Narat range (Figs. 1c and 3). Here, three
141 E–W fault scarps (F3, F4 and F5) are intersected by southward flowing rivers (Fig. 3). At site
142 BBK3, three other fault scarps (F3, F4 and F5) offset four terrace levels (T1 to T4, Figs. 3 A,
143 B and C). Site BBK4 is located ~4 km further east along the strike of fault F3 where two
144 terraces are affected by this fault (Figs. 3D and E). Finally, site BBK5 is located in the eastern
145 part of the basin within a large north–south oriented valley that was entrenched within the
146 Narat range by a tributary of the Kaidu river, which flows toward the center of the
147 Bayanbulak basin (Figs. 1 and 4). Here, one major east–west striking thrust fault (F6) offsets
148 the alluvial deposits of the tributary. We also studied a sixth site (site N) in the Nalati basin on
149 the northern side of the Narat range (Figs. 1 and 5). Here, large recent alluvial fans trapped
150 within the basin have been offset by a major 25 km long E-W striking fault (Fig. 6). In the
151 Yili basin, despite strong evidence for active tectonics, the recent deposition of thick loess
152 (e.g. Yi et al., 2012; Song et al., 2012; Long et al., 2014) has likely changed the original
153 geometry of the morphological markers. We were therefore unable to identify any sites where
154 an accurate estimation of the topographic uplift would be possible.

155 The measured vertical throw, derived fault slip, and horizontal shortenings, together
156 with their uncertainties, are listed in Table 1 for each of the study sites and faulted terraces.
157 Note that at site BBK3 (Fig. 3), we focused our analyses on terraces T2, T3 and T4 because
158 the offset of terrace T1 was too small to be quantified precisely. We also summed the offsets
159 of faults F4 and F5 at this site as the surface traces of these faults are very close together,
160 suggesting that the two faults probably merge at depth. Moreover, as the terrace level cannot

161 be traced south of F3, the uplift measured across this particular fault should be considered a
 162 minimum value. Finally, the offset of terrace T4 is only visible across fault F5 and has not
 163 been preserved elsewhere. Note also that at site BBK4, the small pressure ridges affecting
 164 terraces T1 and T2 on the left bank of the gully (Fig. 3E) are not continuous along strike and
 165 can be considered a second order feature. As such, we neglected these small ridges and
 166 quantified the terrace uplift by considering their large-scale geometries. In the Bayanbulak
 167 basin, vertical offsets preserved by offset geomorphic markers are typically of a few meters to
 168 a few tens of meters. In the Nalati basin, the fault scarps can be much higher, reaching ~45
 169 m.

170

171 4. DATING OF MORPHOLOGICAL MARKERS

172 4.1 Cosmogenic depth profile inversion

173 4.1.1 Principle and theory

174 The abandonment ages of most of the alluvial surfaces were inferred from the depth
 175 distribution of cosmogenic isotope concentrations (e.g. Gosse and Phillips, 2001). In the
 176 general formula of Lal (1991) used to describe the change in ^{10}Be concentration (C) as a
 177 function of depth (Z), the concentration of ^{10}Be also depends on the time since initial
 178 exposure of the surface (in this case, the abandonment of the terrace surfaces) and on the
 179 erosion rate of the surface of the terrace. During the Late Quaternary, the region experienced
 180 strong aridification, which led to widespread deposition of loess over the pre-existing alluvial
 181 deposits (Long et al., 2014; Song et al., 2012; Yi et al., 2012). Thus, erosion of the terraces
 182 was probably very limited. Alternatively, the loess layer may have shielded the underlying
 183 alluvial sediments. To account for potential deposition of loess and/or soil after abandonment
 184 of the terraces, we modified the general equation of Lal (1991) as follows:

$$185 \quad C(z, \varepsilon, t) = \overline{C}_0 \cdot e^{-\lambda \cdot t} + \sum_{i=n, m_1, m_2} \frac{P_i}{\rho \cdot B + \lambda} \cdot e^{\frac{-\rho \cdot z}{\Delta_i}} \cdot \left(1 - e^{-\left(\lambda + \frac{B \cdot \rho}{\Delta_i}\right) \cdot t} \right) \quad (1)$$

186 where B is a "negative" denudation rate (Braucher et al., 2000) that represents the
187 accumulation rate or burial rate since terrace abandonment; t represents the time since initial
188 exposure of the surface (in this case, the abandonment of the terrace surface); C_0 is the
189 average cosmogenic inheritance (in atoms/g); λ is the decay constant of ^{10}Be , equal to
190 $\ln(2)/T_{1/2}$ where $T_{1/2}$ is the half-life (1.387 Ma) (Chmeleff et al., 2010; Korschinek et al.,
191 2010); n , m_1 , and m_2 refer to the neutrons, fast muons and slow muons, respectively; Δ is the
192 attenuation length of neutrons, slow muons or fast muons (~ 160 , ~ 1500 , ~ 4320 g/cm²)
193 (Braucher et al., 2011); P_i is the local production rate (at g⁻¹ yr⁻¹) for the different particles;
194 and ρ is the soil density (g/cm³).

195 This formula does not apply to the sediments deposited during this sedimentation
196 phase. To compute the concentration in these later deposits, it is necessary to assume that the
197 exposure time of each sample is dependent on its depth ($t = z/B$). The equation then becomes
198 (Guralnik et al., 2011):

$$199 \quad C(z, B) = \overline{C}_0 \cdot e^{\frac{\lambda z}{B}} + \sum_{i=n, m_1, m_2} \frac{P_i}{\frac{\rho B}{\Delta_i} + \lambda} \cdot e^{-\frac{\rho z}{\Delta_i}} \cdot \left(1 - e^{-\left(\frac{\lambda}{B} + \frac{\rho}{\Delta_i}\right) z} \right) \quad (2)$$

200 We assume that the few tens of centimeters of loess covering the terraces (Fig. 2)
201 accumulated at a constant rate after terrace abandonment. This assumption is consistent with
202 OSL dating of thick loess sections in the Yili basins (e.g. Song et al., 2012; Long et al., 2014;
203 Yi et al., 2012). Additionally, we calculated end-member age estimates by assuming 1)
204 instantaneous deposition of the entire loess layer immediately after terrace abandonment
205 (maximum age), and 2) very recent deposition of the entire loess layer, meaning that this did
206 not affect the cosmogenic depth profile in the underlying alluvium (minimum age; attenuation
207 in the loess is ignored in such a case).

208 To derive the exposure ages from the depth profiles, we followed a Monte Carlo
209 inversion procedure that tests thousands of parameter combinations to find the best fitting
210 solution by minimizing the difference between the model and the data (e.g. Braucher et al.,
211 2009; Saint-Carlier et al., 2016).

212 The local ^{10}Be production rates for neutrons, fast muons and slow muons were scaled
213 for local latitude and altitude according to Stone (2000), and the local atmospheric pressures
214 were extracted from the ERA40 dataset (Uppala et al., 2005). In this study, we used the SLHL
215 (see level high latitude) production rate of 3.9 ± 0.1 at $\text{g}^{-1} \text{yr}^{-1}$ (compiled by Balco et al. (2009)
216 and revised by Braucher et al. (2011) to include the slow and fast muon contributions). The
217 slow (0.01 at $\text{g}^{-1} \text{yr}^{-1}$) and fast (0.034 at $\text{g}^{-1} \text{yr}^{-1}$) muonic production rates were derived from
218 Braucher et al. (2011). Because the study region is located at high elevation, snow cover
219 could have an impact on the cosmogenic production rate. However, the area is in fact very
220 arid and snow cover is limited to an average of ~ 12 cm during 139 days per year (Yang and
221 Cui, 2005). Moreover, because snow has a very low density ($\sim 0.1 \text{ g cm}^{-3}$), its impact on
222 production rate evaluations can be neglected. Alluvium density was estimated by analyzing
223 photographs of the different outcrops in order to determine the relative proportions of cobbles
224 ($\text{Ø} > 1\text{-}2$ cm) and sand to fine gravels. The bulk density was then calculated by attributing
225 densities of $2.7\pm 0.1 \text{ g/cm}^3$ to the cobbles and $1.9\pm 0.1 \text{ g/cm}^3$ to the sand to fine gravels
226 (Hancock et al., 1999).

227

228 4.1.2 Sampling

229 Sampling for cosmogenic depth profile analyses (Fig. 6 and A) was restricted to the
230 Bayanbulak basin where the loess cover is thinnest. In the Nalati and Yili basins the loess
231 layers are much thicker and the timing of their deposition might be highly variable (e.g. Song
232 et al., 2012; Long et al., 2014; Yi et al., 2012), meaning that the shielding effect cannot be

233 properly corrected for. In the Bayanbulak basin, the sampling sites were carefully selected
234 and the outcrops refreshed to avoid any recent re-exposure (Fig. B). At all sites selected for
235 dating, samples were collected from the surface and from different depths in order to measure
236 the ^{10}Be concentrations in the quartz. We preferentially sampled sand at depth for the
237 cosmogenic dating, however pebbles and cobbles were collected at points near to the surface
238 because the grain size was too coarse and the proportion of sand too low for collection of
239 adequate quantities of sand (Figs. 6 and A in the online depository). At site BBK4, we
240 sampled the highest alluvial surface (T2), which corresponds to a fan deposit. The deposit is
241 composed of mixed sediment, ranging from sand to cobble in grain size, and is quite
242 homogenous across the full thickness that was excavated. The entire site is covered by
243 grassland, in which low vegetation grows on a 15 cm thick soil. Sampling was performed
244 along the most recently eroded part on the modern riser of an incising river (Fig. B) down to
245 ~9.5 m below the surface (Fig. B). In addition, four sand samples were taken at between 35
246 and 200 cm depth and three amalgamated cobbles samples were collected within the 15 cm of
247 soil (Fig. B). At site BBK3, we sampled two alluvial surfaces at different locations: one at T2
248 and one at T3 (Fig. 2). Site BBK3-T2 was sampled on the active riser of the river, and we
249 extracted 4 sand samples at between 45 and 400 cm depth and 2 amalgamated cobble samples
250 that were mixed in the 25 cm of loess deposit (Fig. B). As the BBK3-T3 surface is located far
251 from the river, we dug a hole and collected 5 sand samples at between 30 and 170 cm depth.
252 Both of the BBK3 terraces sampled are composed of mixed sediments ranging from sand to
253 boulder in size. Site BBK1, located in the south, presents two terrace levels that cut through
254 an antecedent anticline. The highest terrace (T2) at site BBK1 was covered by 30 cm of over-
255 bank deposit and 45 cm of loess at the top. We took five samples (between 80 and 280 cm
256 depth) of the sandy fraction within the alluvial material of the terrace (composed of sand to
257 cobble sediment), two samples from the silty part of the terrace and one from the loess part

258 (Fig. B). To collect these samples, we dug a 280 cm deep trench in the terrace riser. The
259 details of the sample treatment and analyses are provided in the online repository.

260

261 4.1.3 Results of the cosmogenic depth profile inversions

262 The results of the cosmogenic analyses are reported in **Table A in the online**
263 **repository**. The cosmogenic depth profiles studied all show a classic exponential decrease in
264 ^{10}Be concentration. The inversions of these profiles (Fig. 6), assuming continuous
265 sedimentation, constrain the mean exposure time of the terraces to 64 ± 6 ka, 22 ± 2 ka, $91\pm 11/9$
266 **ka and $88\pm 7/6$ ka** for the sites BBK4, BBK3-T2, BBK3-T3 and BBK1-T2, respectively
267 (Fig. 6). The hypothesized end-member ages, which assume either instantaneous deposition of
268 loess after terrace abandonment or only recent deposition, bracket these ages to within less
269 than 20 % error (Fig. 6).

270

271 4.2 Single-grain p-IR IRSL dating of loess deposits

272 To better constrain the age of the loess deposit shielding the cosmogenic dated
273 surfaces in the Bayanbulak basin, we also carried out single-grain post-infrared infrared
274 stimulated luminescence (p-IR IRSL) dating of K-feldspar grains (e.g. Thiel et al., 2011). We
275 collected one sample at site BBK1 (Fig. 1) where terrace T2 is covered by a **70 cm** thick layer
276 of loess. The sample was taken immediately above the alluvial deposits at the base of the
277 loess layer (~70 cm below the surface). The silty/loess material was sampled in a metallic
278 pipe and rapidly shielded using black tape. The detail of the ample treatment and
279 measurement are given in the Online repository.

280 The fading-corrected age of the sample constrains the abandonment age of BBK1-T2
281 to 38.7 ± 4.9 ka (Table B and Fig. C). This sample was collected from within the silt/loess
282 cover that caps the terrace deposit and therefore provides a minimum estimate for the timing

283 of terrace abandonment. The IRSL age of ~38 ka is significantly younger than the age derived
284 from the cosmogenic depth profile (Fig. 6). This discrepancy might reveal a complex history
285 of sedimentation/erosion in the time since abandonment of the terrace. Several scenarios are
286 possible, including a hiatus in loess deposition between terrace abandonment at ~88ka to ~38
287 ka characterized by either non-deposition of loess and/or erosion of the river. These
288 uncertainties therefore make it difficult to constrain the true abandonment age of this
289 particular terrace between ~88ka to ~38 ka. At BBK1 and BBK2, the thickness of loess is
290 relatively low and the associated uncertainties are consequently lower. At these two sites, the
291 hypothetical maximum and minimum abandonment ages (calculated by assuming either
292 instantaneous deposition of the entire loess layer immediately after terrace abandonment, or
293 very recent deposition of the loess, respectively) are similar (Fig. 6).

294

295 4.3 Diffusion across fault-scarps

296 4.3.1 Methods

297 We also constrained the ages of some of the terraces that were not sampled for
298 cosmogenic analysis or IRSL dating, by quantifying the fault scarp degradation. The
299 topographic shape of a scarp affecting a terrace surface reflects the interplay between faulting
300 and degradation by erosion. The scarp topography therefore a function of the fault activity
301 and dip, the age of the terrace, and surface processes (Arrowsmith et al., 1998; Avouac and
302 Peltzer, 1993; Nash, 1980). In the absence of gullying or shallow landslide processes,
303 downhill mass transfer across the scarps is generally assumed to occur through diffusion-like
304 processes (i.e. the transfer is assumed to be proportional to the local topographic slope). If the
305 diffusion coefficient that controls the mass transfer efficiency is known, then the scarp profile
306 can be inverted in order to determine/decipher the terrace age. However, unlike terrace risers,
307 the profile of an active tectonic scarp maintains steeper slopes around the piercing point of the

308 fault and by consequence maintains a more triangular (and therefore less gaussian) shape of
309 the slope transverse profile (e.g. Avouac and Peltzer, 1993).

310 In order to unravel the scarp age from diffusional profiles, we built a numerical model
311 based on incremental fault activity with surface rupturing, associated with an interseismic
312 period during which the diffusion erosional processes degrade the refreshed scarp. We
313 assumed that after each rupture, the overhanging part of the scarp collapses vertically onto the
314 the footwall surface. We also assumed that any new ruptures would break the surface at the
315 piercing point of the previous rupture. During interseismic periods, the diffusion equation is
316 solved iteratively through a finite difference scheme. Thus, in our model, the evolution of a
317 given reverse fault scarp depends on five parameters, including 1) the coseismic slip
318 increment, 2) the fault dip, 3) the initial uniform slope of the terrace surface, 4) the time of its
319 abandonment, and 5) the diffusion coefficient. The initial slope of the faulted surface can be
320 estimated from the far field profile elevation across the fault. Based on paleoseismic evidence
321 from active faults further west in Kyrgyztan (Thompson et al, 2002), we considered series of
322 0.5 to 2.5m slips that were generated on a single fault plane dipping at $35\pm 5^\circ$. Though the
323 total deformation rate is greater in this region, the range of slip values considered is large
324 enough to correspond to the eastern part as well. Thus, if either the time of abandonment or
325 the diffusion coefficient is independently known, the other can be determined by adjusting the
326 model to the elevation data using a least square procedure. In both cases, the confidence
327 intervals for the diffusion coefficient or the terrace age were defined by considering a mean
328 square deviation (between the measured elevations and the modeled elevations) within 5 cm
329 of the minimum misfit (see Fig. 4 of Avouac (1993)).

330

331 4.3.2 Calibration of the diffusion

332 The analysed profiles were carefully selected from field observations and satellite
333 image analyses in order to avoid non-diffusive processes across the tectonic scarps, for
334 example shallow landslides with partial scarp collapse, stream incision and gullying, loess
335 deposition, or alluvial fan deposition from a lateral stream along the scarp footwall.

336 In order to calibrate the diffusion coefficients, we selected five fault scarps where the
337 ages of the affected alluvial terrace had already been determined from the cosmogenic depth
338 profile inversion (see example in Fig. 7A and all results in Fig. D in the online depository).
339 These included sites BBK3 and BBK4, where two faults and their associated scarps were
340 analyzed. The calibration results are given in Table 1 and are plotted against the ages of the
341 terraces in Figure 7B. The coefficients range from $8^{+6.6}/_{-3.3}$ m²/ka to $13^{+7.8}/_{-7.3}$ m²/ka with a
342 weighted average value of 10.3 ± 1.4 m²/ka, and do not display any obvious change between
343 the old and young terraces. However, these consistent values are higher than other estimates
344 in the northern Tianshan (Avouac, 1993; Wei et al., 2015), a difference that might be related
345 to variations in the local climate (for example, a colder climate in our study area).

346 In all cases, the whole height of the scarp was considered, including any pressure
347 ridges present at the tops of the scarps (Fig. 7A and Fig. D). The absence of significant
348 variations in diffusion with time or scarp elevation, as well as the low discrepancy, at least
349 within the confidence intervals, between values calculated for the two sites, suggests that, in
350 this particular region, the diffusion processes are relatively steady and are spatially uniform.
351 Even though the analysis above is based on only five profiles, and thus more scarps would
352 need to be included to obtain a higher statistical relevance, we consider these preliminary
353 results to be sufficiently robust to be used for dating other fault scarps.

354

355 4.3.3 Dating fault-scarps and sensitivity of the age inversion

356 The elevation profiles were inverted to date the scarps in the western part of the
357 Bayanbulak basin (BBK2), in the central part of the basin at site BBK3 across fault F5
358 (terrace T4) and at BBK4 across fault F3 (terrace T1), in the eastern part of the basin (BBK5),
359 and finally in the Nalati basin (site Narat1). The results of the profile inversion are presented
360 in Figure 7 and the ages derived from this analysis are given in Table 1.

361 As the morphological dating was based on a series of model assumptions and
362 parameters, we tested the sensitivity of the model by modifying several of these assumptions:
363 multiple instead of single points, the presence of a pressure ridge at the top of the scarp, and
364 non-linear diffusion processes when slopes approach the stability angle of repose (Fig. E). In
365 all of the cases tested, these complexities did not significantly affect our scarp age estimates
366 and in each case, ages were overestimated by no more than 20% (see online depository). The
367 derived slip rates must therefore be considered as minimum values. For the Nalati scarp, the
368 ~1.4 Ma age is much older than in the Bayanbulak basin. On such a time scale, we cannot
369 exclude any changes in diffusion efficiency, or loess deposition, that could have significantly
370 biased our age estimates. However, even if true age would be two or three times younger than
371 the present estimate, the shortening rate would still be limited to a relatively subdued value of
372 ~0.1 mm/yr, a value too low to have a significant impact on the shortening budget across the
373 inner Tianshan.

374

375 **5. DENUDATION RATES FROM COSMOGENIC ANALYSES**

376 The average denudation rate of an entire drainage basin can be estimated by
377 measuring the mean cosmogenic nuclide concentration in a river sand at the basin outlet and
378 estimating the average basin-wide rates of ^{10}Be production (at/g/yr) by neutrons, slow muons
379 and fast muons (Brown et al., 1995).

380 The mean cosmogenic concentration was initially derived from the inherited
381 concentrations derived from the depth profile inversion. These values may represent the

382 average concentrations of cosmogenic nuclides shed by the rivers at the time of terrace fill
383 accumulation. However, the sediments deposited at site BBK1 were transported by the larger
384 Kaidu river, which meanders through the Bayanbulak basin within a large flood plain where
385 complex sedimentrecycling likely occurred. These concerns are also consistent with the
386 higher inherited concentration measured in the BBK1-T2 depth profile (Fig. 6), which
387 suggests a significant contribution of highly concentrated and enriched in ^{10}Be flood plain
388 sediments. As it is difficult to correct for such contamination, we limited our analyses to sites
389 BBK3 and BBK4, where any contamination was likely negligible due to the greater transport
390 distance from the hills. To complement the denudation rates derived from the inherited
391 concentrations, we also collected 3 samples of present-day sand from rivers draining the
392 internal ranges of the Tianshan (Fig. 1C and Fig. F). These samples were treated and
393 measured in the same way as for the depth profile samples, and the results are reported in
394 Table A.

395 In all cases, denudation rates were estimated using present-day cosmogenic production
396 rates. Because the terraces studied are relatively young (Fig. 6) we can assume that the
397 drainage basins have not changed significantly since the accumulation of the terrace fill.
398 However, for site BBK4, the profile was collected in a small gully that cuts the fault scarps
399 and therefore the drainage basin at the time of terrace abandonment is undefined. The present
400 watershed of the closest river is relatively small (11.7 km²) and it is possible that the
401 sediments analyzed actually have originated from an alluvial fan shed from a larger catchment
402 area located to the east, three times bigger than the present one (Fig. D). We therefore
403 considered both of these possibilities in our calculation, though this has little impact on the
404 absolute value of the production rate (Table 2).

405 The basin-scale average cosmogenic production rates were computed in ArcGIS,
406 using an in-house plug-in which averages the local production rates of each point in the study
407 basin. The local production rates were also calculated using a sea level high-latitude (SLHL)
408 ^{10}Be production rate of 3.9 ± 0.1 (compiled by Balco et al. (2009) and revised by Braucher et
409 al. (2011) to include the slow and fast muons contribution), scaled according to Stone (2000)
410 for the local latitude and altitude derived from SRTM at 90 m resolution. We also included a
411 correction factor for shielding by the surrounding topography in our calculations (see Table
412 1). The latter was computed for each individual pixel of the D.E.M. using the ArcGIS(R)
413 tools developed by Codilean et al. (2006), which use a relief shadow modeling technique to
414 identify the area of obstructed radiation.

415 Finally, in order to estimate the uncertainties in the denudation rates, we propagated
416 errors in the cosmogenic production rates and the measured concentrations by assigning an
417 uncertainty of 9 % to the spallogenic production parameters (Balco et al., 2009) and a
418 conservative value of 50 % for both types of muons. The results are reported in Table 2 along
419 with the cosmogenic production rates and correcting topographic factors. In the central
420 Tianshan, our denudation rate estimates range from 0.08 to 0.27 mm/yr (Table 2) with an
421 average of 0.14 ± 0.1 mm/yr. The two paleo-denudation rates at 22 ka (BBK3) and 64 ka
422 (BBK4) are similar to the present-day rates, suggesting no changes in denudation during the
423 late Pleistocene.

424

425 5. DISCUSSION

426 5.1 Shortening rates and the distribution of deformation

427 Using our estimates of the amount of shortening and the terrace abandonment ages, we
428 calculated the shortening rates at each study site (Table1). Over the last ~100 kyr, the total
429 crustal shortening across the Narat range between the Bayanbulak and the Nalati basins
430 reaches 1.36 ± 0.70 mm/yr, suggesting that the shortening accommodated across this internal
431 range represents a significant fraction (possibly at least ~15 %) of the total ~8.5 mm/yr crustal
432 shortening across the entire Tianshan. While our crustal shortening rates should be treated
433 with some degree of caution because of the large uncertainties in the fault dip angles, they
434 would nevertheless remain significant (>0.5 mm/yr) even if the angles of the faults were
435 steeper (60°). Moreover, it is likely that active deformation exists on the southern side of the
436 Yili basin as well (Fig. 5), though the detection of potentially active faults from field
437 observations or satellite images remains difficult here due to the high and rugged topography
438 in this part of the range. The 700 km long Bolokenu-Aqikekuduk (Bo-A) and Kashi river fault
439 zones present additional evidence for Late Quaternary deformation and also experienced
440 strong earthquake activity in the recent past ($M=7.4$ in 1944 and $M=8$ in 1812) (Fang et al.,
441 2014; Shen et al., 2011). These observations support our conclusion that a significant fraction
442 of the active deformation is accommodated within the central part of the Eastern Tianshan.

443 In the Western Tianshan, GPS velocity measurements (Yang et al., 2008) indicate that
444 55 % of the present-day crustal shortening across the range (~20 mm/yr) is distributed along
445 the North and South piedmonts and that 45 % is distributed within the central part of the
446 range (9 mm/yr, Thompson et al., 2002). In the easternmost Tianshan, the distribution of
447 deformation across the range remains unknown but evidence for crustal shortening is also
448 found within the central part where ~1 mm/yr of shortening is accommodated in the Turfan
449 and Yanqi basins (Shen et al., 2011; Huang et al., 2014). Therefore, our the results of our
450 study, together with previous findings, suggest that 15 to 45 % of the total shortening across
451 the range is accommodated by the inner structures.

452

453 5.3 Growth of the Tianshan range: crustal thickening vs. denudation rates

454 Along the transect studied, the eastern Tianshan is around ~270 km wide and the
455 average thickness of the crust on either side of the range is estimated to be ~50 km (Cotton
456 and Avouac, 1994; Poupinet et al., 2002). In assuming a simple 2D conservation mass across
457 the wide range, and also assuming that the width of the range is constant or increases at a
458 negligible rate, a total shortening rate between the Tarim and the Junggar basins of
459 8.5 ± 0.5 mm/yr (Yang et al., 2008) would lead to an average crustal thickening rate of about
460 1.6 mm/yr. It is interesting to compare this value with the rate of erosion at the scale of the
461 entire range. Along the northern and southern Tianshan piedmonts, the average denudation
462 rates derived from cosmogenic analyses in foreland sediments or mass balance in alluvial fans
463 ranged from 0.1 to 0.6 mm/yr during the Late Pleistocene (Charreau et al., 2011; Guerit et al.,
464 2016; Puchol et al., 2016). Therefore, at the scale of the whole range the crustal thickening
465 significantly outpaces the denudation. In the central part of the range, based on the ~1.4
466 mm/yr of shortening accommodated across the Narat range and assuming pure shear
467 deformation distributed over a width of ~50 km (from the center of the Bayanbulak basin to

468 the center of the Nalati basin) and uniformly down to the moho (~50km), we obtain a broadly
469 similar crustal thickening rate of ~1.4 mm/yr across this particular range. This value is ten
470 times greater than the average denudation rate of 0.14 mm/yr that we found in the central part.
471 Therefore, the crustal thickening rate in the Eastern Tianshan is significantly greater than the
472 average denudation rates, at both the regional scale and at the scale of the central part of the
473 range. This disequilibrium is likely due to the arid climate in the region, which possibly limits
474 the denudation (Guerit et al., 2016). The topography of the range has therefore not yet reached
475 steady-state topography: in addition to probable lateral growth by outward propagation of
476 deformation along the southern and northern piedmonts, the range continues to grow mostly
477 by activating internal deformation. Given the difference between the average thickening rates
478 and the average denudation rates, the net growth rate of crustal thickness would therefore be
479 ~1.25 mm/yr, and the mean surface of central Tian Shan would gain 0.2 mm per year or 200
480 m per Myr.

481 The calculated thickening rate across the whole transect of eastern Tianshan range is
482 similar to that calculated across the internal Narat range. This might suggest homogeneous
483 shortening and thickening at the scale of the range. However, to confirm this hypothesis, a
484 complete description of the fault activity across the range, and more importantly a good
485 understanding of the thickening process in the middle and lower crust, by overthrusting,
486 underplating, or viscous flow, would be required. Nevertheless, we note that at the surface,
487 deformation of the inner range seems to preferentially occur along inherited Paleozoic
488 structures and crustal weakness zones that were reactivated during the Cenozoic Indo-Asian
489 orogeny (Dumitru et al., 2001; Jolivet et al., 2010; Poupinet et al., 2002). These structures
490 probably focused the deformation along a number of separated active zones, resulting in the
491 presence of large undeformed areas inbetween these zones (Dumitru et al., 2001; Jolivet et al.,
492 2010). In the case of such strong structural inheritance, the long term crustal shortening of the

493 range could lead to the closure of all intermontane basins in the Tianshan, gradually leading to
494 a state of dynamic equilibrium and steady-state topography. As suggested by a mean surface
495 uplift rate of 200m/Myr, the time needed to reach this equilibrium might be very long due to
496 the very low denudation in this arid region (J.-P. Avouac and Burov, 1996). However, since
497 the Tianshan range is already relatively high and large, it might never reach the final double-
498 vergent wedge shaped morphology, but may instead evolve toward an orogenic plateau due to
499 the thermomechanical strength limit of thickened crust (e.g. Vanderhaeghe et al., 2003).

500

501 **6. CONCLUSION**

502 Our results indicate that in the central eastern part of the Tianshan range the crustal
503 thickening outpaces denudation. This is also likely true at the scale of the whole Tianshan.

504 More systematic estimates of the denudation rates across the range, as well as estimates of the slip rates on
505 several unstudied thrusts, are now required to more precisely estimate the balance between thickening rate and
506 denudation. Moreover, our thickening rates remain first order estimates based on simple 2D conservation mass
507 and simple shear across the range. More accurate calculations in the future should consider sediment recycling
508 and erosion within the piedmont as well as enlargement rate of the range. Nevertheless, the Tianshan appears to
509 represent a reference case of a range experiencing distributed deformation induced by inherited crustal
510 heterogeneities and non-steady-state topographic growth, possibly because of low denudation in this arid region.

511

512 **ACKNOWLEDGMENTS**

513 This study was financed by the French INSU/CNRS SYSTER program. This is CRPG
514 contribution n° **XXXX**.

515

516 **BIBLIOGRAPHY**

- 517 Arrowsmith, J.R., Rhodes, D.D., Pollard, D.D., 1998. Morphologic dating of scarps formed
518 by repeated slip events along the San Andreas Fault, Carrizo Plain, California. *J.*
519 *Geophys. Res.* 103, 10141–10160.
- 520 Avouac, J., Burov, E.B., 1996. Erosion as a driving mechanism of intracontinental mountain
521 growth. *J. Geophys. Res.* 101, 17747–17769.
- 522 Avouac, J.-P., 1993. Analysis of scarp profiles: Evaluation of errors in morphologic dating. *J.*
523 *Geophys. Res.* 98, 6745. doi:10.1029/92JB01962
- 524 Avouac, J.-P., Burov, E.B., 1996. Erosion as a driving mechanism of intracontinental
525 mountain growth. *J. Geophys. Res.* 101, 17747.
- 526 Avouac, J.P., Peltzer, G., 1993. Active tectonics in southern Xinjiang, China: analysis of
527 terrace riser and normal fault scarp degradation along the Hotan-Qira fault system. *J.*
528 *Geophysical Res.* 98, 21773–21807.
- 529 Balco, G., Briner, J., Finkel, R.C., Rayburn, J.A., Ridge, J.C., Schaefer, J.M., 2009. Regional
530 beryllium-10 production rate calibration for late-glacial northeastern North America.
531 *Quat. Geochronol.* 4, 93–107. doi:10.1016/j.quageo.2008.09.001
- 532 Braucher, R., Bourlès, D.L., Brown, E.T., Colin, F., Muller, J.-P., Braun, J.-J., Delaune, M.,
533 Minko, A.E., Lescouet, C., Raisbeck, G.M., Yiou, F., 2000. Application of in situ-
534 produced cosmogenic ^{10}Be and ^{26}Al to the study of lateritic soil development in
535 tropical forest: theory and examples from Cameroon and Gabon. *Chem. Geol.* 170, 95–
536 111.
- 537 Braucher, R., Del Castillo, P., Siame, L., Hidy, A.J., Bourlès, D.L., 2009. Determination of
538 both exposure time and denudation rate from an in situ-produced ^{10}Be depth profile: A
539 mathematical proof of uniqueness. Model sensitivity and applications to natural cases.
540 *Quat. Geochronol.* 4, 56–67. doi:10.1016/j.quageo.2008.06.001

541 Braucher, R., Merchel, S., Borgomano, J., Bourlès, D.L., 2011. Production of cosmogenic
542 radionuclides at great depth: A multi element approach. *Earth Planet. Sci. Lett.*
543 doi:10.1016/j.epsl.2011.06.036

544 Brown, E.T., Stallard, R.F., Larsen, M.C., Raisbeck, G.M., Yiou, F., 1995. Denudation rates
545 determined from the accumulation of in situ produced ^{10}Be in the Luquillo experimental
546 forest, Puerto-Rico. *Earth Planet. Sci. Lett.* 129, 193–202.

547 Charreau, J., Blard, P.H., Puchol, N., Avouac, J.P., Lallier-Vergès, E., Bourlès, D., Braucher,
548 R., Gallaud, A., Finkel, R., Jolivet, M., Chen, Y., Roy, P., 2011. Paleo-erosion rates in
549 Central Asia since 9Ma: A transient increase at the onset of Quaternary glaciations?
550 *Earth Planet. Sci. Lett.* 304, 85–92. doi:10.1016/j.epsl.2011.01.018

551 Charvet, J., Shu, L.S., Laurent-Charvet, S., 2007. Paleozoic structural and geodynamic
552 evolution of eastern Tianshan (NW China): welding of the Tarim and Junggar plates.
553 *Episodes* 30, 162–186.

554 Chmeleff, J., von Blanckenburg, F., Kossert, K., Jakob, D., 2010. Determination of the ^{10}Be
555 half-life by multicollector ICP-MS and liquid scintillation counting. *Nucl. Instruments*
556 *Methods Phys. Res. Sect. B Beam Interact. with Mater. Atoms* 268, 192–199.

557 Codilean, A.T., 2006. Calculation of the cosmogenic nuclide production topographic
558 shielding scaling factor for large areas using DEMs. *Earth Surf. Process. Landforms* 31,
559 785–794.

560 Cotton, F., Avouac, J.P., 1994. Crustal and upper-mantle structure under the Tien Shan from
561 surface-wave dispersion. *Phys. Earth Planet. Inter.* 84, 95–109. doi:10.1016/0031-
562 9201(94)90036-1

563 Dahlen, F.A., Suppe, J., 1988. Mechanics, growth, and erosion of mountain belts, in: Clark,
564 S.P., Burchfiel, B.C., Suppe, J. (Eds.), *Processes in Continental Lithospheric*
565 *Deformation*. Geological Society of America Special Paper, pp. 161–178.

566 Dumitru, T. a, Zhou, D., Chang, E.Z., Graham, S. a, Hendrix, M.S., Sobel, E.R., Carroll,
567 A.R., 2001. Uplift, exhumation, and deformation in the Chinese Tian Shan. *Mem. - Geol.*
568 *Soc. Am.* 194, 71–99. doi:10.1130/0-8137-1194-0.71

569 Fang, L., Wu, J., Wang, C., Wang, W., Yang, T., 2014. Relocation of the 2012 M s6.6
570 Xinjiang Xinyuan earthquake sequence. *Sci. China Earth Sci.* 57, 216–220.
571 doi:10.1007/s11430-013-4755-6

572 Gosse, J.C., Phillips, F.M., 2001. Terrestrial in situ cosmogenic nuclides: theory and
573 application. *Quat. Sci. Rev.* 20, 1475–1560.

574 Guerit, L., Barrier, L., Jolivet, M., Fu, B., Métivier, F., 2016. Denudation intensity and control
575 in the Chinese Tian Shan : new constraints from mass balance on catchment-alluvial fan
576 systems 1106, 1088–1106. doi:10.1002/esp.3890

577 Guralnik, B., Matmon, A., Avni, Y., Porat, N., Fink, D., 2011. Constraining the evolution of
578 river terraces with integrated OSL and cosmogenic nuclide data. *Quat. Geochronol.* 6,
579 22–32. doi:10.1016/j.quageo.2010.06.002

580 Hancock, G.S., Anderson, R.S., Chadwick, O.A., Finkel, R.C., 1999. Dating fluvial terraces
581 with ¹⁰Be and ²⁶Al profiles: application to the Wind River, Wyoming. *Geomorphology*
582 27, 41–60.

583 Jolivet, M., Dominguez, S., Charreau, J., Chen, Y., Li, Y., Wang, Q., 2010. Mesozoic and
584 Cenozoic tectonic history of the central Chinese Tian Shan: Reactivated tectonic
585 structures and active deformation. *Tectonics* 29, 1–30. doi:10.1029/2010TC002712

586 Korschinek, G., Bergmaier, A., Faestermann, T., Gerstmann, U.C., Knie Rugel, G., K.,
587 Wallner, A., Dillmann, I., Dollinger, G., Lierse von Gosstowski, C., Kossert, K., Maiti,
588 M., Poutivtsev, M., Remmert, A., 2010. A new value for the ¹⁰Be half-life by Heavy-Ion
589 Elastic Recoil detection and liquid scintillation counting. . *Nucl. Inst. Meth. B* 268, 187–
590 191.

591 Lal, D., 1991. Cosmic ray labeling of erosion surfaces: in situ nuclide production rates and
592 erosion models. *Earth Planet. Sci. Lett.* 104, 424–439.

593 Long, H., Shen, J., Tsukamoto, S., Chen, J., Yang, L., Frechen, M., 2014. Dry early Holocene
594 revealed by sand dune accumulation chronology in Bayanbulak Basin (Xinjiang, NW
595 China). *The Holocene* 24.

596 Nash, D.B., 1980. Morphological analysis of degraded normal fault scarps. *J. Geol.* 88, 353–
597 360.

598 Poupinet, G., Avouac, J.-P., Jiang, M., Wei, S., Kissling, E., Herquel, G., Guilbert, J., Paul,
599 A., Wittlinger, G., Su, H., Thomas, J.-C., 2002. Intracontinental subduction and
600 palaeozoic inheritance of the lithosphere suggested by a teleseismic experiment across
601 the Chinese Tien Shan. *Terra Nov.* 14, 18–24.

602 Puchol, N., Charreau, J., Blard, P., Lavé, J., Dominguez, S., Pik, R., Saint-carlier, D., ASTER
603 Team, 2016. Limited impact of Quaternary glaciations on denudation rates in central
604 Asia. *Geol. Soc. Am. Bull.*

605 Reigber, C., Michel, G.W., Galas, R., Angermann, D., Klotz, J., Chen, J.Y., Papschev, A.,
606 Arslanov, R., Tzurkov, Ishanov, M.C., V.E., 2001. New space geodetic constraints on
607 the distribution of deformation in the Central Asia. *Earth Planet. Sci. Lett.* 191, 157–165.

608 Saint-Carlier, D., Charreau, J., Lavé, J., Blard, P.H., Dominguez, S., Avouac, J.P., Wang, S.,
609 Arnold, M., Aumaître, G., Keddadouche, K., Léanni, L., Chauvet, F., Bourlés, D.L.,
610 2016. Major temporal variations in shortening rate absorbed along a large active fold of
611 the southeastern Tianshan piedmont (China). *Earth Planet. Sci. Lett.* 434, 333–348.
612 doi:10.1016/j.epsl.2015.11.041

613 Shen, J., Wang, Y., Li, Y., 2011. Characteristics of the Late Quaternary right-lateral strike-
614 slip movement of Bolokenu-Aqikekuduk fault in northern Tianshan Mountains, NW
615 China. *Geosci. Front.* 2, 519–527. doi:10.1016/j.gsf.2011.05.004

616 Song, Y., Li, C., Zhao, J., Cheng, P., Zeng, M., 2012. A combined luminescence and
617 radiocarbon dating study of the Ili loess, Central Asia. *Quat. Geochronol.* 2–7.

618 Stone, J.O., 2000. Air pressure and cosmogenic isotope production. *J. Geophys. Res. - Solid*
619 *Earth* 105, 23753–23759.

620 Tapponnier, P., Molnar, P., 1979. Active faulting and cenozoic tectonics of the Tien Shan,
621 Mongolia, and Baykal regions. *J. Geophys. Res.* 84, 3425–3459.

622 Thiel, C., Buylaert, J., Murray, A., Terhorst, B., Hofer, I., Tsukamoto, S., Frechen, M., 2011.
623 Luminescence dating of the Stratzing loess profile (Austria) and testing the potential of
624 an elevated temperature post-IR IRSL protocol. *Quat. Int.* 234, 23–31.
625 doi:10.1016/j.quaint.2010.05.018

626 Thompson, S.C., Weldon, R.J., Rubin, C.M., Abdrakhmatov, K., Molnar, P., Berger, G.W.,
627 2002. Late Quaternary slip rates across the central Tien Shan, Kyrgyzstan, central Asia
628 107. doi:10.1029/2001JB000596

629 Uppala, S.M., Kållberg, P.W., Simmons, A.J., Andrae, U., Bechtold, V.D.C., Fiorino, M.,
630 Gibson, J.K., Haseler, J., Hernandez, A., Kelly, G.A., Li, X., Onogi, K., Saarinen, S.,
631 Sokka, N., Allan, R.P., Andersson, E., Arpe, K., Balmaseda, M.A., Beljaars, A.C.M.,
632 Berg, L. Van De, Bidlot, J., Bormann, N., Caires, S., Chevallier, F., Dethof, A.,
633 Dragosavac, M., Fisher, M., Fuentes, M., Hagemann, S., Hólm, E., Hoskins, B.J.,
634 Isaksen, L., Janssen, P.A.E.M., Jenne, R., McNally, A.P., Mahfouf, J.-F., Morcrette, J.-J.,
635 Rayner, N.A., Saunders, R.W., Simon, P., Sterl, A., Trenberth, K.E., Untch, A.,
636 Vasiljevic, D., Viterbo, P., Woollen, J., 2005. The ERA-40 re-analysis. *Q. J. R.*
637 *Meteorol. Soc.* 131, 2961–3012. doi:10.1256/qj.04.176

638 Vanderhaeghe, O., Medvedev, S., Fullsack, P., Beaumont, C., Jamieson, R. a., 2003.
639 Evolution of orogenic wedges and continental plateaux: insights from crustal thermal-
640 mechanical models overlying subducting mantle lithosphere. *Geophys. J. Int.* 153, 27–

641 51. doi:10.1046/j.1365-246X.2003.01861.x

642 Wei, Z., Arrowsmith, J.R., He, H., 2015. Evaluating fluvial terrace riser degradation using
643 LiDAR-derived topography: An example from the northern Tian Shan, China. *J. Asian*
644 *Earth Sci.* 105, 430–442. doi:10.1016/j.jseas.2015.02.016

645 Willett, S.D., Slingerland, R., Hovius, N., 2001. Uplift, shortening, and steady state
646 topography in active mountain belts. *Am. J. Sci.* 301, 455–485.

647 Wu, C., Wu, G., Shen, J., Chen, J., Alimujiang, Chang, X., 2014. The Late Quaternary
648 activity of the Nalati Fault and its implication for the crustal deformation in the interior
649 of the Tianshan mountains. *Igarss 2014* 1–5. doi:10.1007/s13398-014-0173-7.2

650 Yang, Q., Cui, C., 2005. Impact of climate change on the surface water of Kaidu River Basin.
651 *J. Geogr. Sci.* 15, 20–28.

652 Yang, S., Jie, L.I., Qi, W., 2008. The deformation pattern and fault rate in the Tianshan
653 Mountains inferred from GPS observations 51. doi:10.1007/s11430-008-0090-8

654 Yi, C.E., Lai, Z.P., Sun, Y.J., Hou, G.L., Yu, L.P., Wu, C.Y., 2012. A luminescence dating
655 study of loess deposits from the Yili River basin in western China. *Quat. Geochronol.* 10,
656 50–55. doi:10.1016/j.quageo.2012.04.022

657

658

659

660

661

662

663

664

665

666 **Figure captions:**

667 **Figure 1:** A: structural map of the eastern Tianshan (GPS velocities relative to stable Eurasia from
668 Yang et al., 2008). B: interpretative cross section. C: Geological map of the Bayanbulak basin. In
669 Figure 1c, the labels 1, 2, 3, 4 and N refer to the study site and to Figures 2A, 2B, 3A, 3B, 4 and
670 6 in the main text, respectively. D: Interpretative cross section of the Bayanbulak basin. E:
671 Topographic slope attitudes across the eastern Tianshan. Elevation data were extracted from the 1
672 arc second SRTM dataset, along a N10°E 10 km stacked profile crossing the Bayanbulak and
673 eastern termination of the Yili basin.

674 **Figure 2:** satellite images of sites BBK1 (A) and BBK2 (B) and DGPS elevation profile on both sites
675 projected onto a line perpendicular to the fault scarps (C). In BBK1 the elevations are given
676 relative to the Kaidu river. The star and the colored lines indicate the location of the cosmogenic
677 depth measurement and the topographic profiles, respectively.

678 **Figure 3:** A: Satellite image of site BBK3 (Fig.1C for location). B: DGPS elevations relative to the
679 river that formed the alluvial surfaces at site BBK3 (projected onto a line perpendicular to the
680 fault scarps). C: Field photograph of the western river bank at site BBK3 showing the different
681 terrace levels. D: Satellite image of site BBK4 (see Fig.1C for location). E: B: DGPS relative
682 elevations to the river of the alluvial surfaces in site BBK4 (projected onto a line perpendicular to
683 the fault scarps). The stars and the colored lines indicate the location of the cosmogenic depth
684 measurement and the topographic profiles, respectively.

685 **Figure 4:** Satellite image of the tributary valley located in the eastern part of the Bayanbulak basin,
686 where alluvial deposits are offset by fault F6. The enlargement shows the site studied (BBK5) and
687 the location of the DGPS profile (not corrected from the regional slope) shown in the inset
688 diagram above. The red line indicates the locations of the topographic profiles.

689 **Figure 5:** A: Topographic map of the Nalati and Yili basins (see box 6 in Fig 1C). The black arrows
690 indicate active tectonic scarps associated with south dipping reverse active faults. The white line
691 shows the location of a 4 km long stacked topographic profile. B: Panorama and DGPS profile of
692 a cumulated fault scar within the Nalati basin that has been uplifted by 60 m (see location in
693 figure DA). C: 4 km long stacked topographic profile across the Nalati and Yili basin. D:
694 Panorama of the southern border of the Nalati basin and Narat Range, displaying active fault
695 scarps.

696 **Figure 6:** ^{10}Be cosmogenic concentrations as a function of depth for each of the four sites analyzed.
697 Note that all of the fine sediments (silt, loess, soil) were considered to have a bulk density of
698 $1.6\pm 0.2 \text{ g/cm}^3$ and that their real thicknesses were converted to a theoretical thickness
699 corresponding to the densities of the respective terraces. The inset diagrams show the misfit plots
700 for both the age and inheritance values.

701 **Figure 7:** Diffusion analyses of the fault scarps. A: Calibration of the diffusion coefficient
702 across fault F3 at site BBK3. The diagram shows the changes in elevation measured
703 across the studied fault scarps using DGPS (black crosses). The blue dashed line shows
704 the best fit model determined using the least squares procedure. The inset diagram to the
705 right provides the misfit variations (calculated difference between the modeled
706 topographic profiles and the observed elevations) against the diffusion coefficient k . The
707 inset diagram to the right compares the observed slope (filled circles) to the best-fit
708 modeled slope (in blue) across the scarps. B: Diffusion coefficient k against the ages of
709 the uplifted terraces. C to G: Topographic profile inversions used to date the scarps.

710 **Figure 8:** Geological cross sections and balance between crustal thickening and denudation
711 across the entire Tianshan and Narat ranges.

712 **Tables**

713 **Table 1:** Age, uplift and shortening rates for each of the deformed surfaces dated in the
714 study.

715 **Table 2:** Denudation rate data, including the basin average cosmogenic production rates and
716 topographic factors, the inherited concentrations of ^{10}Be derived from the cosmogenic
717 depth profiles, and the calculated denudation rates.

718

719

720

721

722

723

724
725

Table 1

Offset terrace/DGPS profile	Cosmogenic or IRSL age	Uplift	K	Diffusion age	Uplift rate	Slip	Horizontal shortening	Slip rate	Horizontal shortening rate
	(ka)	(m)	(m ² /ka)	(ka)	(mm/yr)	(m)	(m)	(mm/yr)	(mm/yr)
BBK1 Fault 1									
T2	88±6/7		n.a		0.11±0.02		14±5	0.19±0.06	0.15±0.06
T2 _(IRSL)	39±5	9.5±1	n.a		0.24±0.05	17±5	14±5	<u>0.42±0.14</u>	<u>0.35±0.15</u>
							mean:	0.31±0.1	0.25±0.1
BBK2 Fault 2									
Profile west		11±2		158±30/80	0.07±0.04	19±6	16±6	0.12±0.07	0.1±0.06
Profile east		7±1		84±30/50	0.08±0.05	12±4	10±4	<u>0.15±0.1</u>	<u>0.12±0.09</u>
							mean:	0.13±0.08	0.11±0.07
BBK3 Fault 3 (south)									
T2	22±2	3±0	8±3.3/6.6		0.14±0.02	5±2	4±2	0.24±0.07	0.19±0.08
T3	91±9/11	17±3	12±3.6/7.5		0.19±0.04	30±9	24±10	<u>0.33±0.1</u>	<u>0.27±0.11</u>
							mean:	0.28±0.09	0.23±0.1
BBK3 Fault 4 (center) & Fault 5 (north)									
T2	22±2	6±1	13±7.3/7.8		0.27±0.05	10±3	9±3	0.48±0.14	0.39±0.16
T3	91±9/11	18±3	12±3.8/4.9		0.2±0.04	31±9	26±10	<u>0.34±0.11</u>	<u>0.28±0.12</u>
							mean:	0.41±0.13	0.34±0.14
BBK3 Fault 5									
T4		25±4		103±54/61***	0.25±0.14	44±11	36±14	0.42±0.25*	0.35±0.23*
BBK4 Fault 3									
T1		3.5±1		13±7/6	0.27±0.15	6±2	5±2	0.47±0.29	0.38±0.26
T2	64±6	11±2	9±2.2/4.2		0.17±0.03	19±6	16±6	<u>0.3±0.09</u>	<u>0.25±0.1</u>
							mean:	0.38±0.19	0.31±0.18
							mean of fault 3**:	0.33±0.14	0.27±0.14
BBK5 Fault 6									
		9±1		54±17/19	0.17±0.06	16±5	13±5	0.29±0.13	0.24±0.13
Nalati basin									
Profile Narat1E		45±7		1393±249/268	0.03±0.01	78±23	64±26	<u>0.06±0.02</u>	<u>0.05±0.02</u>
							Total:	1.66±0.72	1.36±0.71

*not included in the total

**includes sites BBK3 and BBK4

***inverted using local calibration of K from terraces BBK3-T2 and BBK3-T3

726
727
728
729
730
731
732
733
734
735
736
737

738
739

Table 2

Watershed	Average Altitude (m)	Topographic factor	Production rates			Denudation rate (mm/yr)
			Neutrons (at g ⁻¹ y ⁻¹)	Slow muons (at g ⁻¹ y ⁻¹)	Fast muons (at g ⁻¹ y ⁻¹)	
Paleo-denudation from inherited concentration in terraces						
BBK4 bv1 (64 ka)	3071	0.998	37.94	0.03	0.06	0.12±0.01
BBK4 bv2 (64 ka)	3166	0.995	39.99	0.03	0.06	0.13±0.01
BBK3-T2 (22ka)	3155	0.996	39.73	0.03	0.06	0.13±0.01
Present denudation from river bed samples						
Yili	2694	0.995	31.07	0.03	0.06	0.27±0.03
BBK	3155	0.996	39.73	0.03	0.06	0.08±0.00
BBKS	3404	0.992	45.71	0.04	0.07	0.12±0.01

740

Figure1
[Click here to download high resolution image](#)

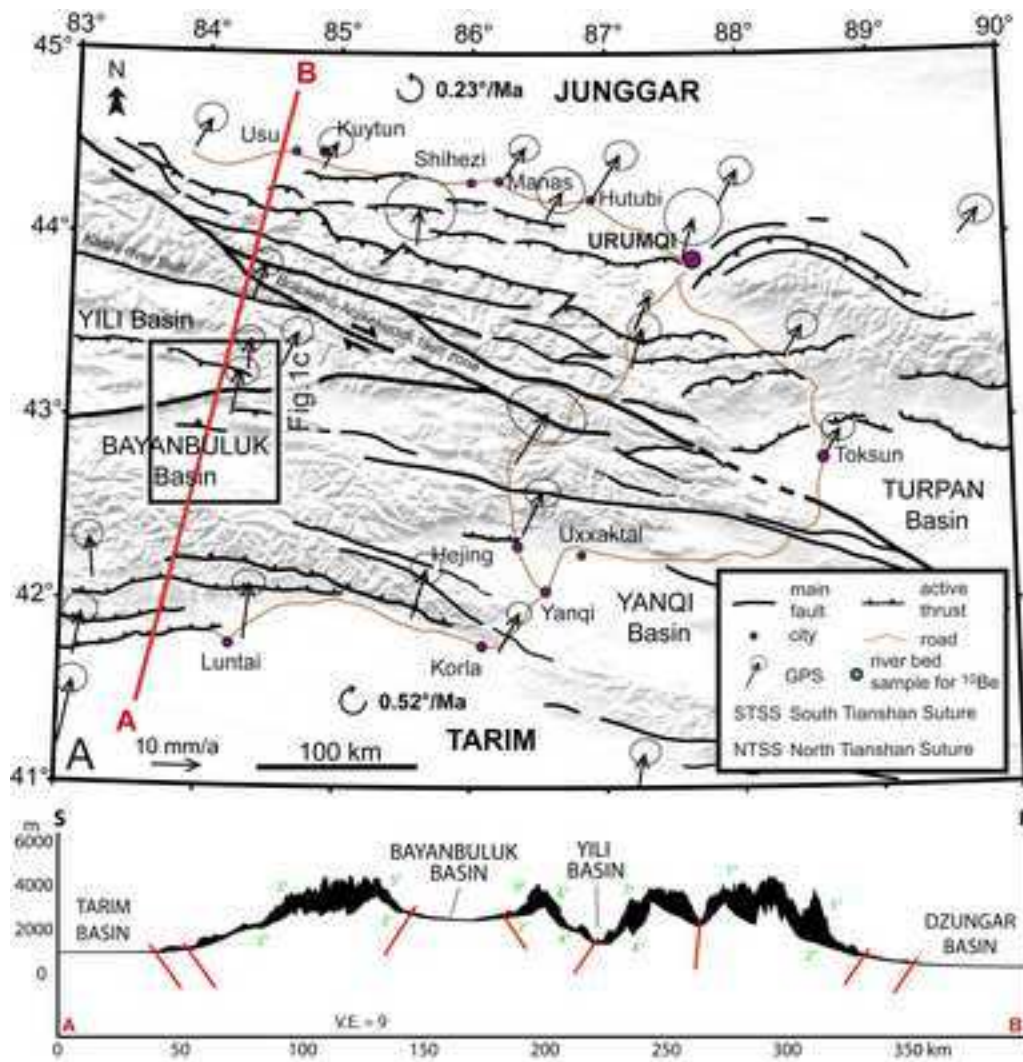


Figure 1

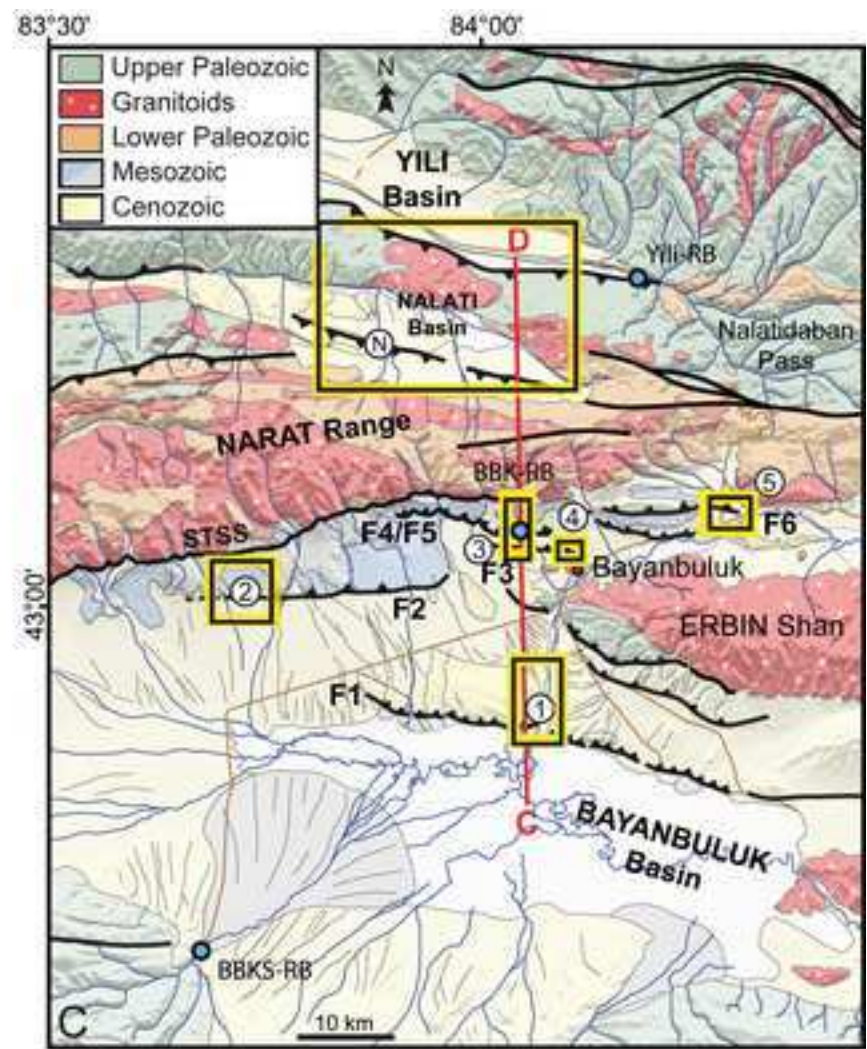


Figure 2

Figure2
[Click here to download high resolution image](#)

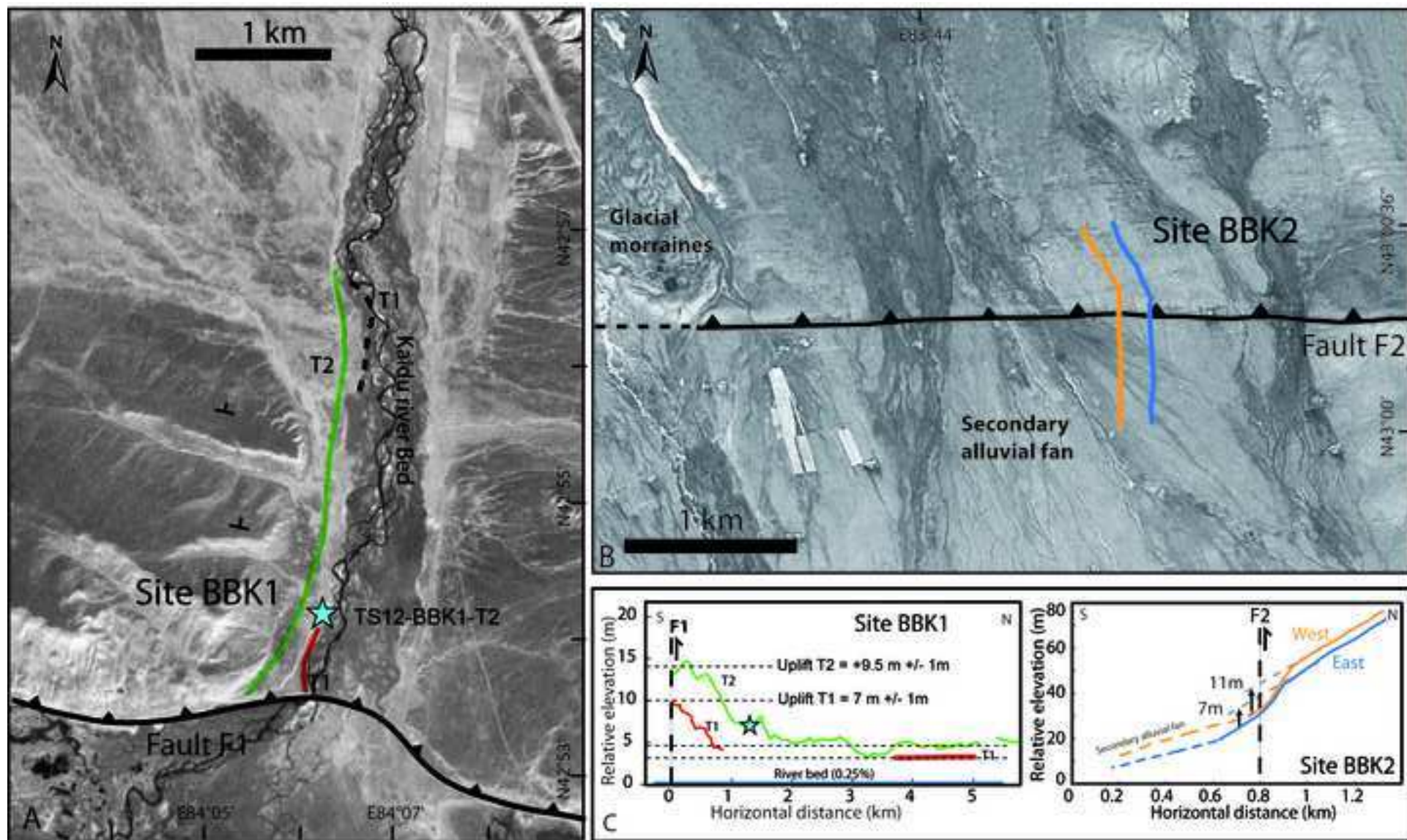


Fig. 2

Figure3
[Click here to download high resolution image](#)

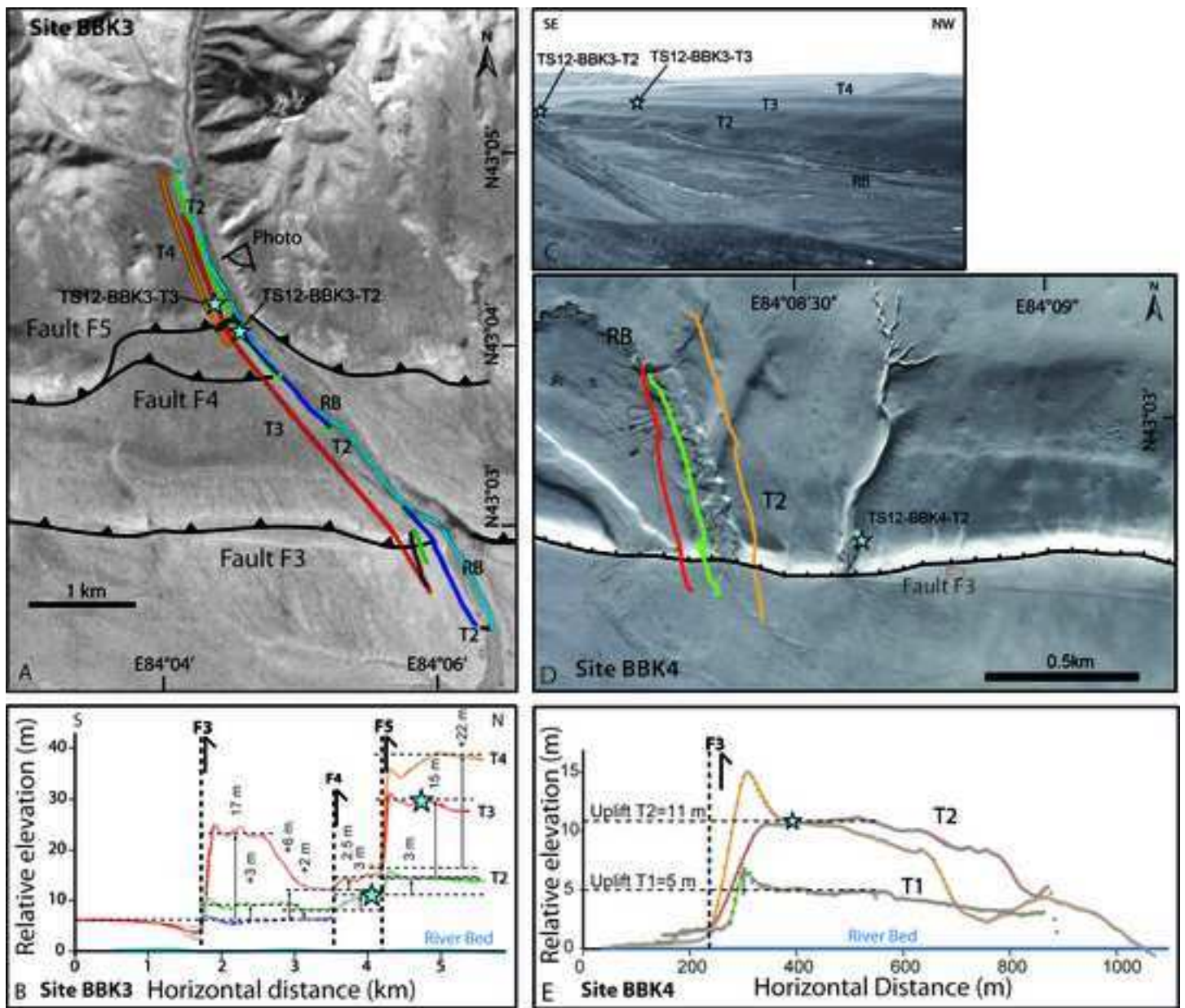


Fig. 3

Figure4

[Click here to download high resolution image](#)

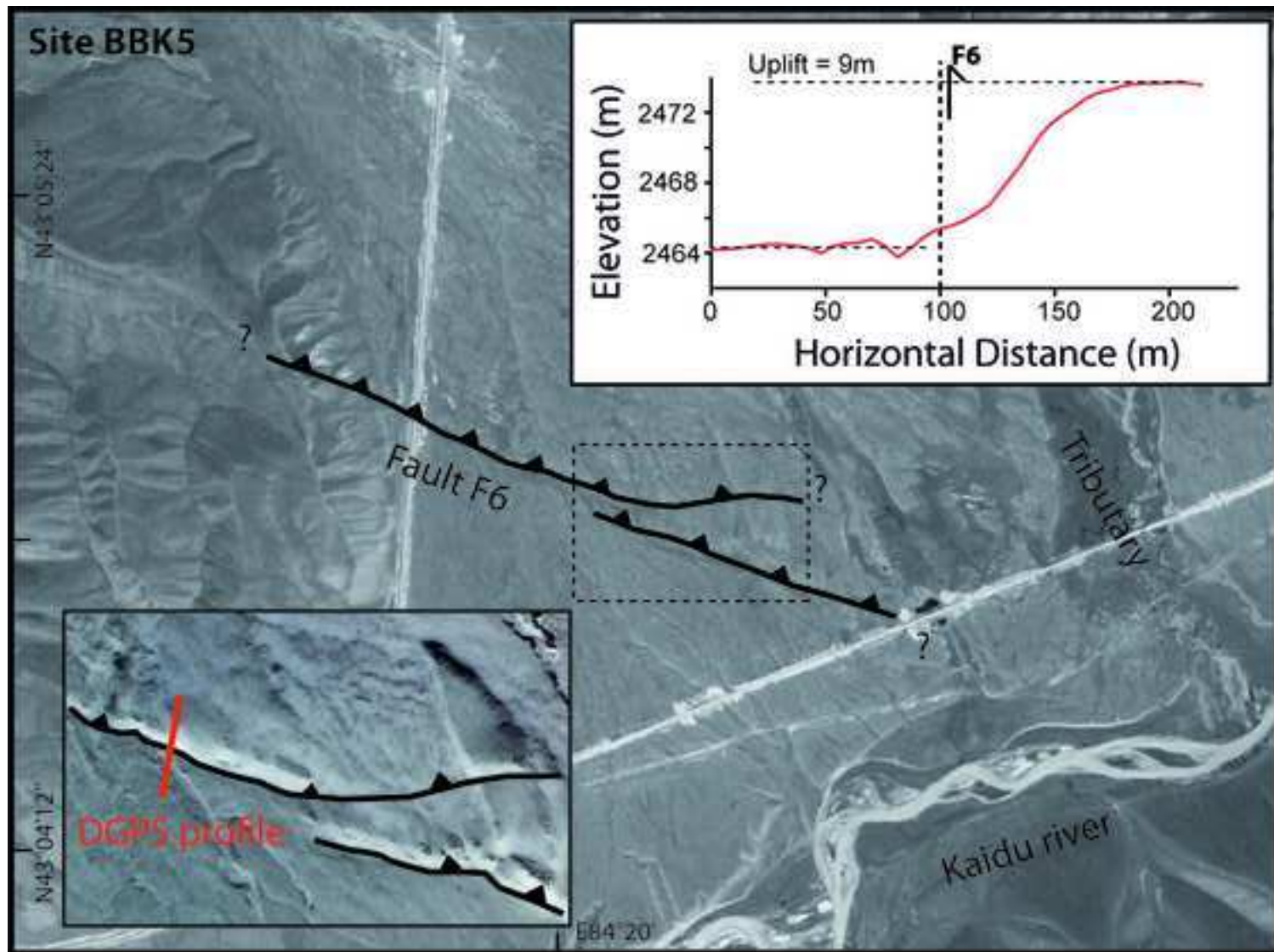


Fig. 4

Fig. 5

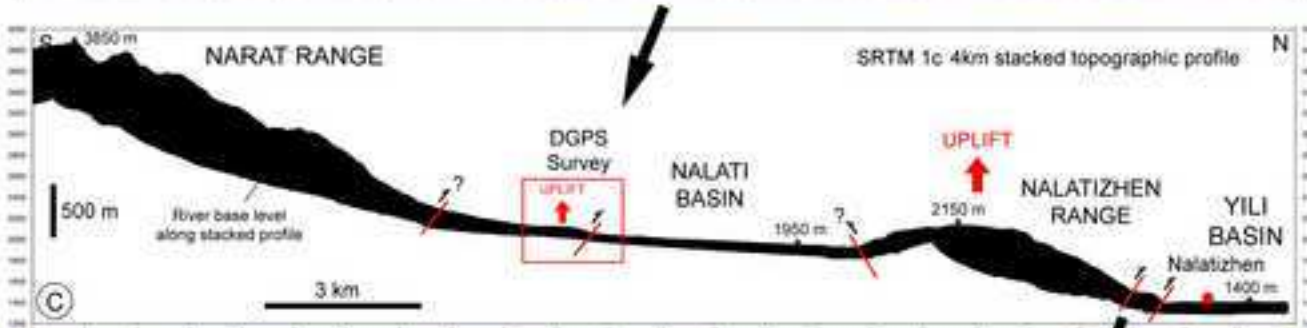
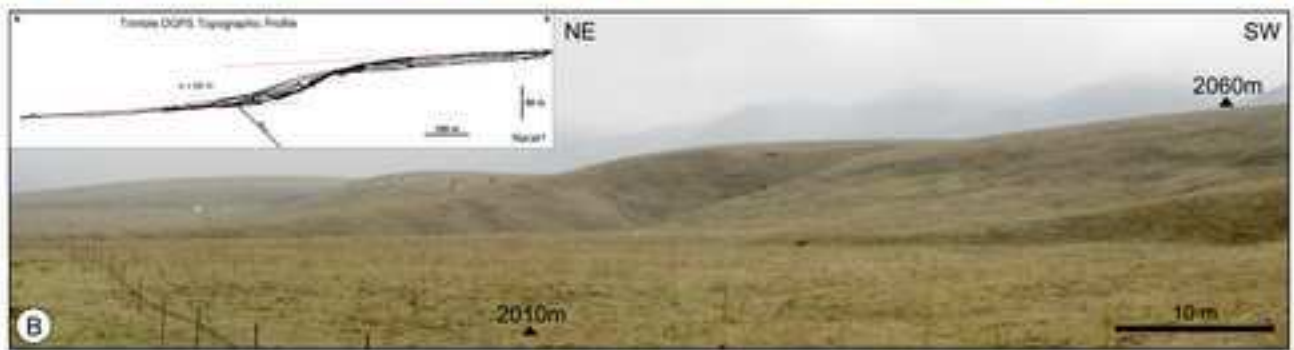
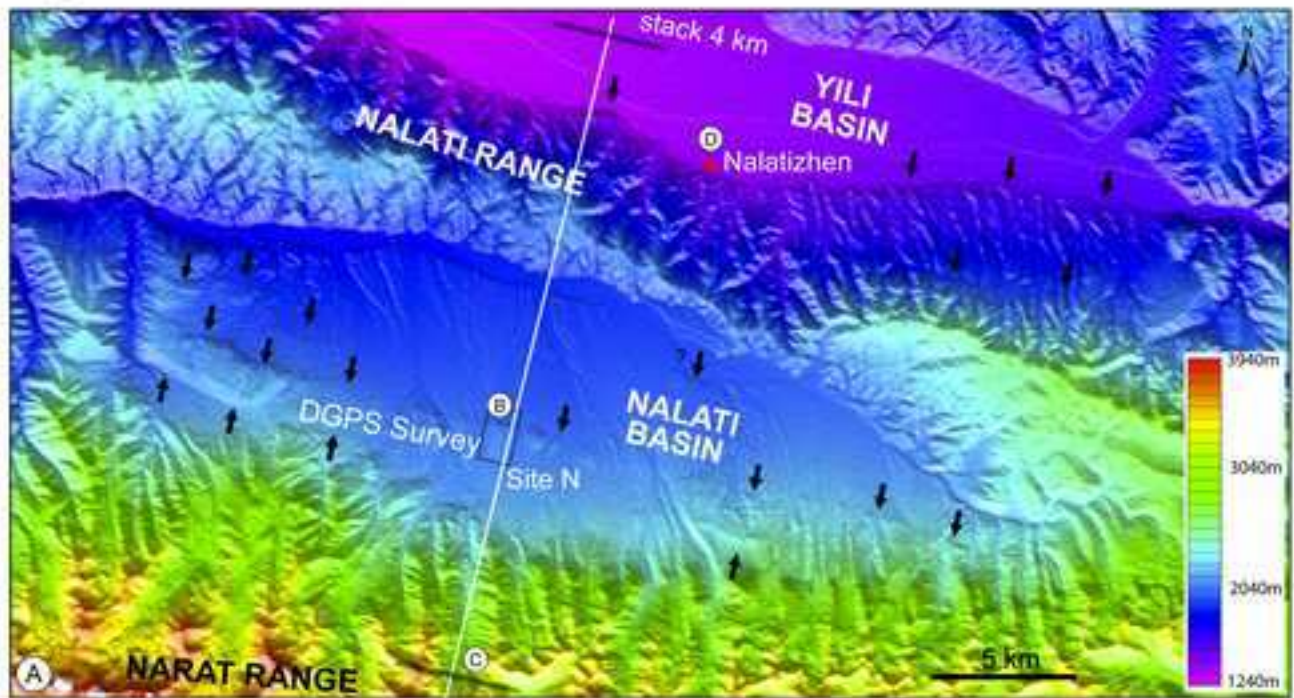


Figure6
[Click here to download high resolution image](#)

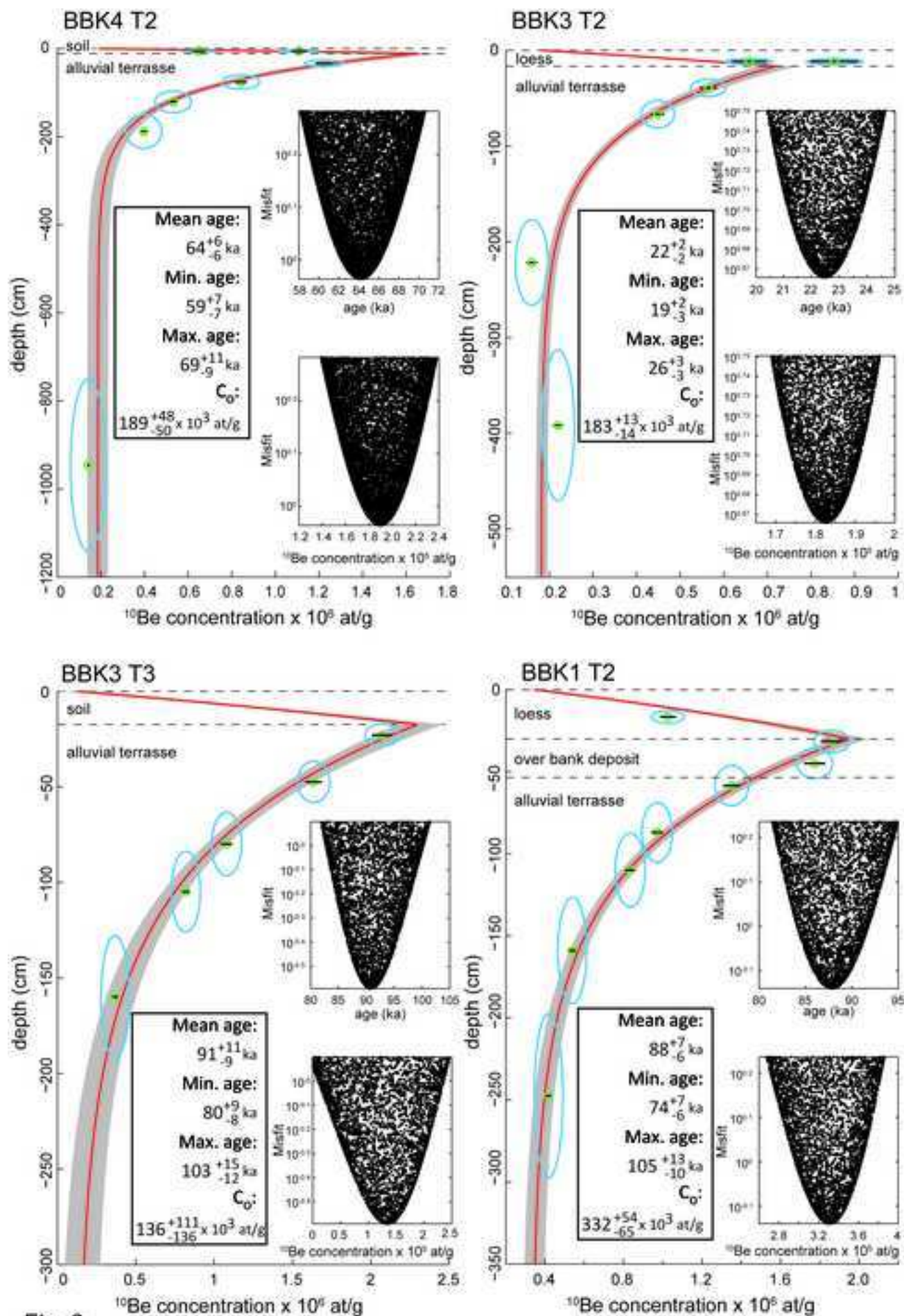


Fig. 6

Figure 7
[Click here to download high resolution image](#)

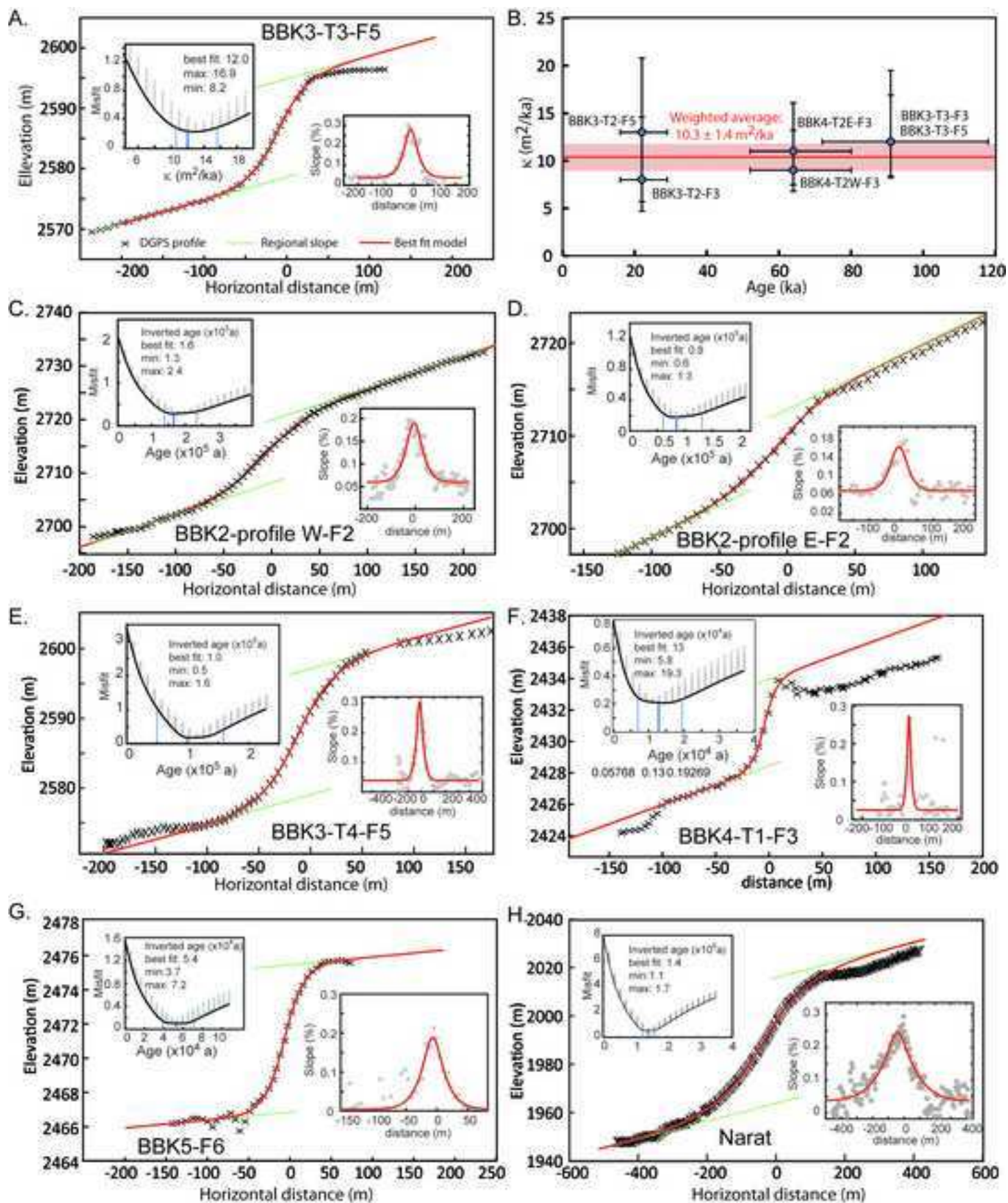


Fig. 7

Figure8

[Click here to download high resolution image](#)

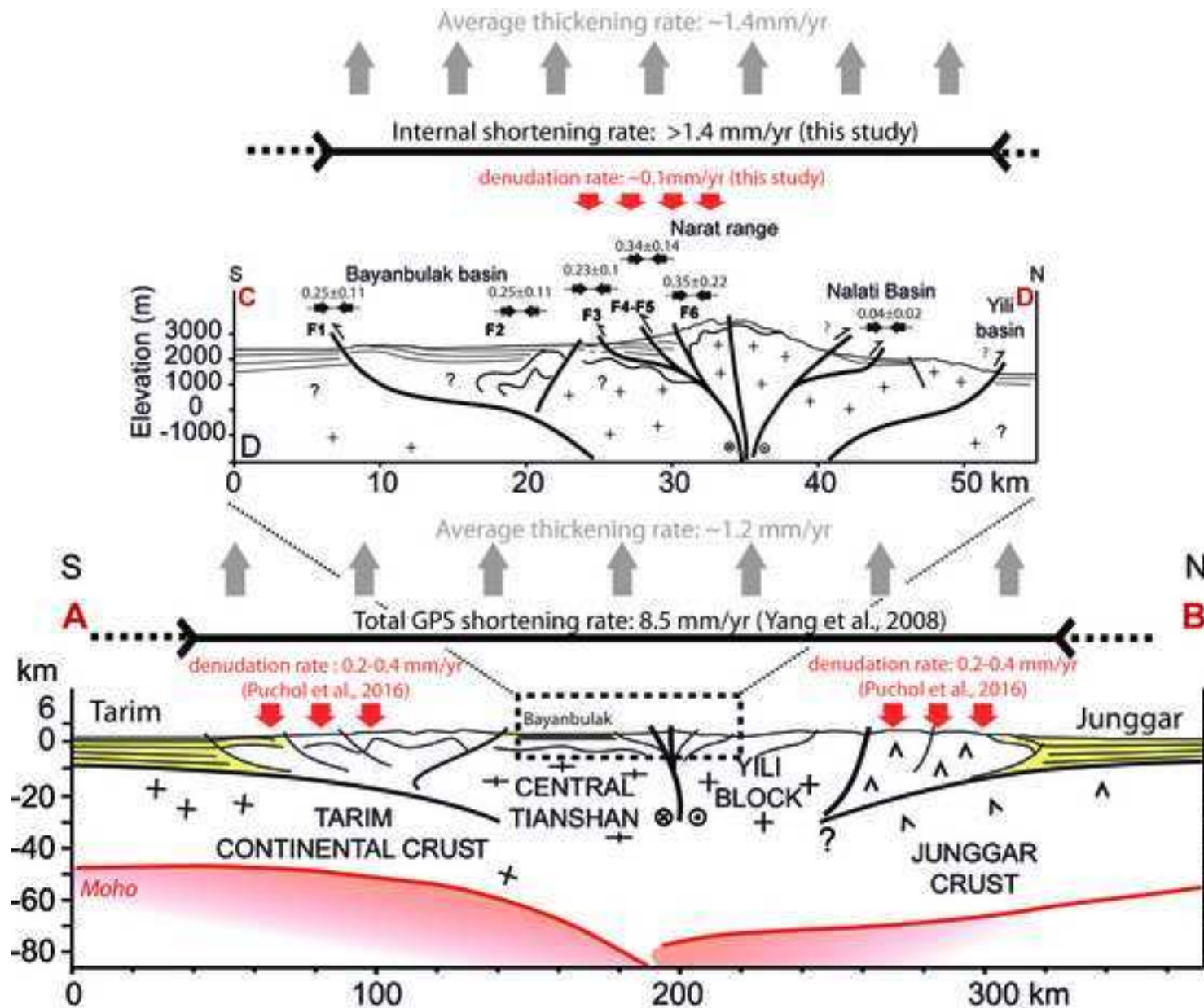


Fig. 8

Supplementary material for online publication only

[Click here to download Supplementary material for online publication only: Online_repository_BBK_final_revised.docx](#)